BMC Cancer

RESEARCH Open Access

Impact of irradiation conditions on therapy of Lewis lung carcinoma in mice using glucose-ethylenediamine carbon dots

Pavlo Lishchuk[1,2], Halyna Kuznietsova[1,2], Taisa Dovbynchuk[1], Nataliia Dziubenko[1,2], Liudmyla Garmanchuk[1], Sergei Alekseev[1,2], Mykola Isaiev[3], Nataliya Pozdnyakova[4], Artem Pastukhov[4], Nataliya Krisanova[4], Tatiana Borisova[2,4], Vladimir Lysenko[5] and Valeriy Skryshevsky[1,2*]

Abstract

Background nowadays, the photoacoustic imaging is in the mainstream of cancer theranostics. In this study the nanoparticles with previously proven photoacoustic imaging properties, i.e. glucose-ethylenediamine carbon dots (GE-NPs), were tested for photoacoustic cancer therapy.

Methods nanoparticle biocompatibility was analyzed in cell toxicity and neurotoxicity experiments ex vivo. Biochemical parameters were analyzed in animal experiments in vivo after intramuscular implantation of Lewis Lung carcinoma cells into the C57/Black mouse line.

Results GE-NPs at concentrations of 0.1–1.0 mg/ml did not change the extracellular level, exocytotic and transporter-mediated release, as well as the initial rate of uptake and accumulation of L-[^{14}C]glutamate in isolated rat brain nerve terminals. GE-NP-treated mice had evidence of the probable protection of the liver and attenuating the systemic consequences of tumor growth, as evidenced by normalization of serum aspartate aminotransferase (ASAT), and lactate dehydrogenase (LDH) levels, compared to vehicle-dosed tumor-bearing animals. According to hematological analysis, treatment with GE-NPs caused an increase in red blood cells and hematocrit up to the healthy control levels. When a combination of GE-NPs (1 mg/ml) is injected into a mouse tumor and the tumor is irradiated by a laser beam, it leads to an increase in mice survival by more than 30% compared to GE-NPs-treated non-irradiated mice, and a decrease in the growth rate of the cancerous tumor. The observed therapeutic effect can be related to the photoacoustically-induced destruction of cancer cells significantly enhanced by the presence of the incorporated GE-NPs, because the laser-induced localized heating of mice skin has not exceeded 2 °C.

Conclusions the efficiency of photoacoustic therapy of Lewis Lung carcinoma in mice using biocompatible carbon dots was demonstrated. Biocompatible GE-NPs own multimodal potential in cancer theranostics, including both photoacoustic imaging and therapy, by applying different irradiation conditions.

Keywords Carbon dots, Glucose-ethylenediamine, Photoacoustic therapy, Lung carcinoma, Mice

*Correspondence:
Valeriy Skryshevsky
skryshevsky@knu.ua

Full list of author information is available at the end of the article

Introduction

The global cancer burden is growing, and the projected cancer burden increase in 2050 is predicted to be over 35 million new cancer cases which is a 77% increase from the estimated 20 million cases in 2022 [1]. The use of nanoparticles (NPs) for cancer treatment may overcome the disadvantages of most common cancer therapies (surgery, radiation, chemotherapy, hormonal therapy) [2–10]. There are several ways of NP targeting the cancer cells; i.e. passive targeting (NPs are applied to organism without specific targeting agents) and active targeting (small drug molecules are attached to NPs to assist its accumulation in cancer cells). Due to enhanced permeability and retention effect (EPR effect), NPs can leave the blood capillaries of the tumor, consisting of underdeveloped and leaky endothelium, and remain in the tumor for days. NPs can be administrated either intratumoral or intravenous, for passive or active targeting [6, 11–15].

Among different types of NPs, carbon-based fluorescent nanomaterials, such as graphene quantum dots [16, 17], graphene oxide [18–20], and carbon dots (CDs) [21, 22] have attracted significant attention because of their unique optical and biocompatible traits under physiological conditions. Such characteristics are greatly beneficial for various biomedical applications, such as theranostics. Compared to traditional anticancer models, the combination of diagnosis and therapy can gather more detailed information for precise, high-sensitivity, and low-interference cancer treatment. The integration also can monitor the metastasis and relapse of tumor to obtain high therapeutic efficiency. Hence, a large variety of theranostic agents based on multicomponent nanomaterials that combine two or more imaging functions (e.g., fluorescence and /photoacoustic imaging) and therapeutic modalities have been studied, and many valuable results have been obtained in preclinical animal experiments on various tumor models [23, 24].

CDs own aromatic and aliphatic regions, constituents of which are graphene, graphene oxide and diamond [25]. Water-suspended CDs possess inorganic carbon cores with sp2 hybridized graphene islands and diamond-like sp3 hybridized inclusions. The shells of CDs are of amorphous carbon and oxygen-containing polar groups, such as carbonyls, carboxyls, and hydroxyls. CDs exhibit not only fluorescent imaging capability but also a phototherapy nature including photodynamic therapy (PDT) and photothermal therapy (PTT), which is beneficial to photothermal and photoacoustic imaging. CDs provide a strong potential for multimodal imaging and multiple therapies leading to promote the practical applications of CDs in the nanomedical fields [26]. Also, CDs with potential uses for the administration of drugs against cancer are considered advantageous systems to control drug release in the organism and increase the efficiency of treatments and reduce their toxicity [27–30].

CD can be applied for (i) photodynamic therapy (PDT) electronically excited photosensitizer transfers energy to the ground state of molecular oxygen to produce excited singlet oxygen, which is cytotoxic, thus leading to direct tumor cell death via apoptosis or necrosis and damage of the tumor microvasculature and dramatic changes in tumor microenvironment [31–35]; (ii) photothermal cancer therapy (PTT) that typically employs near-infrared (NIR) light-absorbing agents that convert laser energy into heat to kill cancer cells, generating irreversible cellular damage and subsequent tumor destruction; and (iii) ultrasound hyperthermia. Ultrasound is the sound waves that can propagate from one soft tissue to another (except bone tissue junction) and to get the vibration back from soft tissues, a high-intensity focused ultrasound was used [36]. The major physical effects of ultrasound are the generation of heat, mechanical vibration, and cavitation.

A photoacoustic approach can share characteristic features of both PTT and ultrasound hyperthermia. Literature data revealed that the photoacoustic approach was used mainly for imaging, and there are not numerous data regarding therapy [37–39]. This study aimed to assess an efficacy of photoacoustic therapy using CDs. Mechanical vibration of CDs can initiate cavitation leading to cancer cell damage [6, 40]. Ultrasound (UlS) is a kind of non-toxic mechanical wave commonly used in clinical diagnostic imaging, which can also play a therapeutic role in tumor eradication. This efficient treatment method utilizes the UlS to activate sonosensitizers to generate toxic reactive oxygen species (ROS) to eradicate tumor cells [41–43]. Compared with traditional PDT, UlS offers a significant advantage due to its deep penetration depth [44]. Furthermore, it allows for targeted tumor ablation through rapid ultrasonic energy deposition, destroying tumor blood vessels and cancer cells while sparing surrounding healthy tissues cells [41, 42, 45].

Here, we have developed approaches for cancer therapy using acoustic wave generation in carbon NPs under photo-induced treatment of Lewis lung carcinoma in mice (Scheme 1). This technique is based on the fact that some materials, such as CDs, can generate detectable acoustic waves after laser irradiation [46, 47]. To create a treatment protocol using the generation of an acoustic wave in CDs that were injected into the tumor, it was necessary to select the type of CDs, their concentration in the buffer solution, the parameters and mode of laser operation (wavelength, pulse frequency, energy density), the protocol for the introduction of CDs and irradiation of the tumor, etc. It was necessary to select CDs with optimal acoustic properties (maximum amplitude of the generated acoustic wave) so that the used CDs

Scheme 1 Roadmap of the experiments

concentration would be non-toxic and laser irradiation would not lead to the effect of hyperthermia.

According to our previous research, glucose-ethylenediamine nanoparticles (GE-NPs) demonstrate low toxicity and high photoacoustic response [21, 48] Chemical structure of these nanoparticles consisted of O–H and N–H functionalities, methylene groups, conjugated C = C and C = N double bonds, as well as single C–O bonds. The most intense signals in their ^{1}H-NMR spectrum relates to –HC(OH)– protons of hydroxylated hydrocarbon chains of cross-linked glucose molecules (2.5–4 ppm), presence of which resulted in hydrophilicity of GE-NPs and their high solubility in water.

Taking into account all aforementioned, the GE-NPs seems promising as agents for photoacoustically-induced cancer treatment. So, the aims of the present study were: (1) to synthesize the GE-NPs ; (2) to assess their size, zeta potential, and photoacoustic signal for tissue phantoms; (3) to analyze neurotoxicity of GE-NPs ex vivo using isolated rat brain nerve terminals and measuring the extracellular level, exocytotic and transporter-mediated release and uptake of L-[^{14}C]glutamate, the main excitatory neurotransmitter in the central nervous system; (4) to assess anticancer activity of GE-NPs without irradiation in experiments in vivo using mice with Lewis lung carcinoma; (5) to perform photoacoustic therapy of mice with Lewis lung carcinoma using GE-NPs (Scheme 1).

Methods and materials

Synthesis of GE-NPs

The GE-NPs were synthesized using a procedure, similar to the one, described in [49]. Glucose monohydrate (0.495 g, 2.5 mmol) and ethylenediamine (170 µL, 2.5 mmol) were dissolved in 5 mL of water and sealed in a teflon-lined stainless-steel autoclave. The autoclave was heated to 180 °C with a 5 °C·min^{-1} heating rate, kept for 3 h at this temperature and naturally cooled. The resulted solution was evaporated at 60 °C in a rotary evaporator and dried at 60 °C under 10^{-3} bar vacuum. The solid was dissolved in water (1 mg·ml^{-1}) under sonication. The resulting transparent dark-brown solution was centrifuged at 14,500 g for 10 min, negligibly small precipitate was disposed.

GE-NPs were used in neurotoxicity studies for ex vivo experiments at concentrations ranging from 0.1 to 1.0 mg/ml. 100 µl of the GE-NP suspension (with a concentration of 1 mg/ml) was injected into the mouse in the experiments in vivo.

Post-synthesis characterization of GE-NPs

Dynamic light scattering

Size distribution measurements of diluted colloidal solutions of GE-NPs were performed using Zetasizer Nano ZS from Malvern Instruments (He–Ne laser 633 nm, 5mW, with 173° Non-Invasive Back Scatter (NIBS) detector and narrow band filter).

Photoacoustic measurements

The light radiation from a Q-switched Nd: YAG laser with laser fluency equal to 300 mJ/cm^2, laser beam focus ~ 2 mm and in the irradiation mode "532 nm (green) + 1064 nm (IR)" was used as an excitation source. The pulse energy was reduced by a filter to avoid any tissue damage. Additionally, the intensity of the laser beam was controlled with a photodiode. The beam was directed toward a photoacoustic probe to the studied tissue. The photoacoustic probe comprised a transparent glass buffer (30 mm thick) and a piezoelectric sensor rigidly attached to it. A transmission gel was used to couple the photoacoustic buffer to the tissue phantom. Excited photoacoustic signals were registered from the target sample (located 15 mm beneath the surface), using a piezoelectric ring, then amplified and detected by a digital oscilloscope. The final oscillogram was averaged among 128 pulses.

Biocompatibility study of GE-NPs: neurotoxicity assessment ex vivo of GE-NPs using isolated rat brain nerve terminals

Ethical approval of ex vivo experiments using rats

During the ex vivo study on neurotoxicity, male Wistar rats with a body weight of approximately 120 g were housed in the animal facilities at the Palladin Institute of Biochemistry, National Academy of Sciences of Ukraine. They were kept in a temperature-controlled room (22–23 °C) with access to water and dry food pellets

ad libitum. The experiments were performed in accordance with the Guidelines of the European Community (2010/63/EU), local laws and policies, and approved by the Animal Care and Use Committee of the Palladin Institute (Protocol # 3 from September 21, 2020). The studies were stated in accordance to the ARRIVE guidelines for reporting experiments involving animals [50, 51]. A total of 12 animals were used in the study.

Nerve terminals (synaptosomes) from the rat brain cortex

The cortex regions were isolated from the brains of decapitated animals. Then they were quickly removed, and homogenized in the ice-cold solution containing 0.32 M sucrose, 5 mM HEPES-NaOH, pH 7.4, and 0.2 mM EDTA. Synaptosome preparation was isolated from one animal, and each record of the experimental data was performed in triplicate. Synaptosomal preparations were obtained by differential and density gradient (using Ficoll-400) centrifugations of the brain homogenates according to Cotman`s method with slight modifications [52–54]. Synaptosomal isolation procedures were performed at + 4 °C. All experiments used synaptosomal suspensions for 2–4 h after isolation. The standard salt solution contained (in mM): NaCl 126; KCl 5; $MgCl_2$ 2.0; NaH_2PO_4 1.0; HEPES 20, pH 7.4; and D-glucose 10. Ca^{2+}-containing media were supplemented with 2 mM $CaCl_2$, and Ca^{2+}-free media were supplemented with 2 mM EGTA. Protein concentrations were analyzed according to [55].

The exocytotic and transporter-mediated release, and the extracellular level of L-[^{14}C] glutamate in the nerve terminal preparations

Glutamate is the main excitatory neurotransmitter in the central nervous system. When the transport of glutamate is impaired and there is an excess of glutamate in the synaptic cleft, it leads to neurotoxicity and neuronal death due to overexcitation of postsynaptic glutamate receptors. Synaptosomal preparations were diluted in the standard salt solution up to a concentration of 2 mg of protein/ml, and after pre-incubation at 37 °C for 10 min were pre-loaded with L-[^{14}C]glutamate (2.81 μM, 1 μCi/ml) in standard salt solution at 37 °C for 10 min. After loading, the synaptosomal suspensions were washed with 10 volumes of ice-cold standard salt solution and the pellets were re-suspended to achieve a concentration of 1 mg of protein/ml. Synaptosomal suspensions (125 μl; 0.5 mg of protein/ml) were pre-incubated at 37 °C for 10 min, then aliquots of GE-NPs at concentrations of 0.1, 0.5 and 1.0 mg/ml were added and pre-incubated with synaptosomes for 6 min, and then sedimented using a microcentrifuge (20 s at 10,000 *g*). The extracellular synaptosomal level of L-[^{14}C]glutamate was measured in Ca^{2+}-free media. Transporter-mediated synaptosomal release of L-[^{14}C]glutamate was initiated with 35 mM KCl in Ca^{2+}-free media and measured for 6 min. Exocytotic synaptosomal release of L-[^{14}C]glutamate in Ca^{2+}-containing media was stimulated by the membrane depolarization with 35 mM KCl and was measured at 6 min time point and calculated by subtraction of L-[^{14}C]glutamate release in Ca^{2+}-containing media from that in Ca^{2+}-free one. The extracellular level and release of L-[^{14}C]glutamate were measured in the aliquots of the supernatants (100 μl) and the pellets using liquid scintillation counting with Sigma-Fluor® High Performance LSC Cocktail (1.5 ml) and liquid scintillation counter Hidex 600SL (Finland), and their values were expressed as percentage of total accumulated L-[^{14}C]glutamate [25]. L-[^{14}C]glutamate release data were collected from several independent triplicated experiments using different synaptosome preparations (n).

The initial rate and accumulation of L-[^{14}C] glutamate by the nerve terminals

Transporter-mediated uptake of L-[^{14}C]glutamate by synaptosomes was measured in the synaptosomal suspensions (125 μl of suspension, 0.4 mg of protein/ml) that were pre-incubated in the standard salt solution at 37 °C for 6 min with the GE-NPs at concentrations of 0.1, 0.5 and 1.0 mg/ml. The uptake was initiated by the application of L-glutamate/L-[^{14}C]glutamate (10 μM/450 nM, 0.167 μCi/ml). Synaptosomes were incubated at 37 °C for 1 min (the initial rate) and 10 min (the accumulation) and then sedimented in a microcentrifuge (20 s at 10,000×*g*). Non-specific L-[^{14}C]glutamate binding was assessed in immediately cooled samples after the addition of radioactivity. L-[^{14}C]glutamate uptake was calculated based on the decrease in radioactivity in the supernatant aliquots (100 μl) and the increase in radioactivity in the SDS-treated pellets. L-[^{14}C]glutamate uptake was calculated with liquid scintillation counting using Sigma-Fluor® High Performance LSC Cocktail (1.5 ml) and liquid scintillation counter Hidex 600SL (Finland) [25]. L-[^{14}C] glutamate uptake data were collected from several independent experiments in triplicate performed using different synaptosome preparations (n).

Administration of GE-NPs in vivo using lung cancer mice model

Ethical approval of in vivo experiments using mice

In vivo testing, animals were bred in-house and kept in the animal facility of Taras Shevchenko National University of Kyiv in standard conditions (natural light, 50% humidity at 20-22ºC) and free access to standardized rodent diet and tap water. All experimental procedures were conducted according to the Declaration of Helsinki ("Scientific Requirements and Research Protocols" and "Research Ethics Committees"). Experimental protocols

were approved by the University's Animal Care and Use Committee (Protocol from 3/09 to 2018).

Anticancer treatment of LLC-bearing mice using GE-NPs without irradiation

C57BL6 male mice 12–14 weeks old with an initial body weight of 21.5 ± 2.5 g were used in the experiments. A highly metastatic Lewis lung carcinoma cells (LLC) in C57BL6 mice were employed. Suspension of primary tumor cell culture got from LLC tumor in the amount of 1×10^6/100 µL in saline, with a volume of 100 µl, was injected subcutaneously into the right flank of each animal. This number of inoculated cells results relatively fast tumor growth, which allows to estimate the effect of the treatment on tumor volume before achieving the allowed maximum (2500 mm^3 [56]) without being compromised with animal mortality due to metastases burden. After tumors reach approx. 100 mm^3 (6-7th day post-inoculation), mice were randomized on groups according to tumor volume, and the treatment was started and continued for 18 days as daily intratumoral injections of GE-NPs (concentration 1 mg/mL, volume of administration 5 mL/kg, dose 5 mg/kg) in $NaHCO_3$ buffer served as a vehicle. The rationale of repeated administrations was to investigate the effects of GE-NPs itself on tumor growth dynamics. Two mutually perpendicular tumor diameters were measured every day before treatment. Length (L) (the larger diameter), and width (W) (smaller diameter) were used to calculate the tumor volume (V) according to the formula: V = (W^2 x L) x 0.5 mm^3.There were 2 groups of mice ($n = 3$): one group was treated with a vehicle, and the other was treated with GE-NPs (5 mg/kg, approximately 0.1 ml per mouse). A healthy control group consisting of mice without tumor inoculation was also included. After 18 days of treatment, the mice were sacrificed under 2,2,2-tribromoethanol (150 mg/kg) anesthesia, and their tumors were weighed; and lung metastases were also counted. Hematological and blood serum biochemical analyses were performed after the sacrifice as well. Thus, aspartate aminotransferase (ASAT), alanine aminotransferase (ALAT), lactate dehydrogenase (LDH), gamma-glutamyl transferase (GGT), alkaline phosphatase (ALP), creatinine and urea in the blood serum were determined using commercial kits according to the manufacturer's instructions (Cormay, Poland). Hematological analysis was performed using the hematology analyzer MCL-3124 (Guangzhou Mecan Trading Co., Ltd, China).

Anticancer treatment of LLC-bearing mice using GE-NPs and irradiation

For this study, tumor transplantation was performed in the same way but in the amount of 0.5×10^6cells per animal (average animal weight at the beginning of the experiment was 19.4 ± 1.7 g). This number of cells injected results in more slowly tumor growth, which provides appropriate time to metastases development and allows to assess animal survival due to that. The introduction of nanoparticles (5 mg/kg, approx. 0.1 ml per mice) or a saline as the vehicle control was performed once on the 10th day after tumor inoculation intratumorally when tumors reached approx. 100 mm^3 and after the mice were randomized to the treatment groups (according to tumor volume). Tumor irradiation was performed 15 min after the treatment, and continued for 5–10 min. Both irradiated and non-irradiated controls were included. $N = 4–5$ for Vehicle-treated groups (either irradiated or non-irradiated), and $n = 6–7$ for GE-NPs-treated groups (either irradiated or non-irradiated).The rationale of this scheme was to investigate the effect of GE-NPS after being activated with irradiation. Since the procedure was supposed to have a dramatical effect on further tumor growth, it was performed once.

When irradiating mice, an Alvi Prague TL-500 laser was used with a nozzle in the irradiation mode "532 nm (green) + 1064 nm (IR)", as well as a set of 3 neutral density (ND) filters along the route laser pulses. The pulse repetition rate is 1 Hz. The duration of each pulse is 3.5 ns, and the beam diameter is (3 ± 1) mm. The energy density of the outgoing laser pulse (without filters) is 30 mJ / cm^2, about 30% of the energy is from green "532 nm", 60% of the energy is from IR "1064 nm" of the component, respectively, and up to 10% is due to loss, reflection and so on. The filters transmitted an energy density of approximately 2.5 mJ/cm^2, wherein the near-infrared component, predominantly at 1064 nm, accounted for up to 90% of the total transmitted energy. The transmittance of the filters was calculated analytically based on the Bouguer – Lambert – Beer law. In a given mode of laser exposure to the tumor, a modulated localized heating of the body surface of the mouse ≤ 2°C was observed throughout the entire exposure time. Temperature changes were monitored using a Seek Thermal Imager (Compact Pro model).

Taking into account relatively low absorption level of the NIR radiation by colloidal GE-NPs themselves [21], 10% o the green light was intentionally used to significantly amplify resulted photo-acoustic signal [48] generated by tumor labeled with GE-NPs and thus, to guarantee the laser-induced therapeutic effect reported in our manuscript. Therefore, weekly absorbed NIR radiation represents major part (90%) of the whole combined laser intensity while highly absorbed green radiation was limited only at 10% of the global intensity.

After irradiation, tumors were measured as described above.

The survival of animals in the experimental groups was determined relative to the appropriate control until the natural death of the animals. Animals expressed signs of

toxicity which require humane killing were euthanized, and considered as those which died. Clinical signs to define humane endpoints include [57, 58]: (1) Signs of dehydration or emaciation (weight loss more than 15% during 72 h), (2) Persistent hypothermia, (3) Blood-stained or mucopurulent discharge from any orifice, (4) Deep/heavy respiration, (5) Hind-limb paralysis or weakness, (6) Diarrhoea over a 48-h period, (7) Tumors that interfere with locomotion or cause abnormal vocalization, animal behavior or functions, (8) Necrosis resulting in skin breakdown or exudation.

Statistical analysis

The neurotoxicity experimental data ex vivo using rat brain nerve terminals were stated as the mean ± S.E.M. of *n* independent experiments. One-way ANOVA was used to assess the extracellular level, exocytotic release, transporter-mediated release, and uptake of L-[^{14}C]glutamate in nerve terminal preparations. The Shapiro-Wilk procedure was used to test normality in samples and Levene's test was used to verify the homogeneity of variance for the groups ($p > 0.05$) before applying ANOVA.

For mice experiments, homogeneity of variance was assessed using the Levene test. The data was analyzed using one-way or two-way analysis of variance (ANOVA) with the Tukey post hoc test. We evaluated animal survival using the Log-rank Mantel–Cox test and further depicted the results using a Kaplan-Meier plot. A p-value of less than 0.05 was considered statistically significant.

Study limitations

Small sample size of in vivo experiments might compromise the statistical power of the results. However, such sample size was chosen as it was a pilot study and according to 3R rules. Then given the differences in tumor growth dynamics and mortality between the studies with and without irradiation, it appears that the mechanisms driving the antitumor efficacy of the two tested approaches also differ. Further, more extended studies would be required to explore and clarify these underlying mechanisms.

Results

Physical and chemical properties of GE-NPs

Diameters and zeta potential of GE-NPs

The GE-NPs were characterized by dynamic light scattering (DLS) and electrophoretic light scattering (ELS), using Malvern Zeta-sizer instrument. According to the DLS data (Fig. 1a), the solution of GE-NPs contains large particles (52 ± 14 nm). According to our previous data [21], more than 75% of the GE-NPs pass through 20 kDa membrane, so the particles are rather small, while the value of 52 nm could be explained by micelles or other aggregates formation in GE-NPs solution. Despite this fact and slightly negative zeta potential (ζ = -18,6 mV) of GE-NPs (Fig. 1b), the solution of GE-NPs is stable in time (no precipitate formed under centrifugation of the solution, stored for at least 2 weeks). Probably, the solution stability is caused by GE-NPs hydrophilicity due to the presence of hydroxylated hydrocarbon chains of cross-linked glucose molecules in their structure.

Photoinduced UIS generation enhanced by GE-NPs

The generation of a photoacoustic response involves three key steps:

1. Absorption of radiation: the target object absorbs the incident radiation.

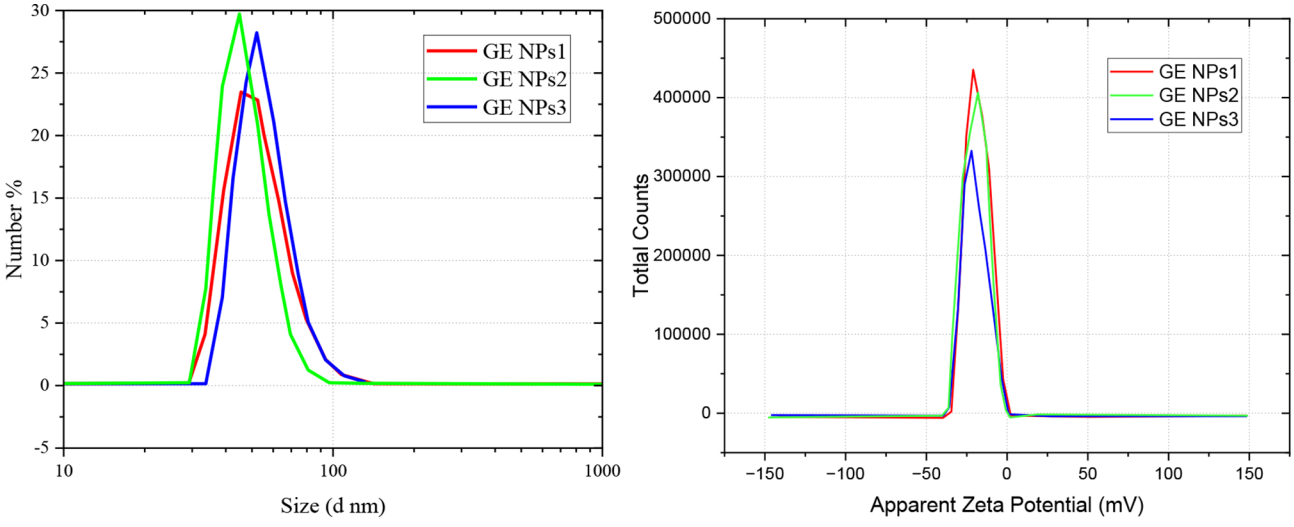

Fig. 1 GE-NPs size distributions by number, found by the DLS (**a**) and zeta-potential distributions by ELS (**b**). Three measurements (for 1 min each) were performed for 5 mg/ml aqueous dispersion of GE-NPs nanoparticles

2. Thermal conversion: the absorbed radiation is converted into heat energy, causing a localized temperature increase.
3. Thermoelastic expansion: the increase in temperature leads to thermal expansion of the material, resulting in the generation of acoustic waves.

Following a short laser pulse excitation, the local fractional volume expansion dV/V of the heated tissue at position $\vec{r}$ can be expressed as follows [59]:

$$\frac{\Delta V}{V} = -k\Delta\, p\,(\vec{r}) + \beta\, \Delta\, T\,(\vec{r}) \qquad (1)$$

,

where k is the isothermal compressibility, β is the thermal coefficient of volume expansion, $\Delta\, p\,(\vec{r})$ and $\Delta\, T\,(\vec{r})$, are changes in pressure and temperature, respectively. The isothermal compressibility is equal to ~5 × 10 −10 Pa^{-1} for water or soft tissue, the thermal coefficient of volume expansion is equal to ~4 × 10 −4 K^{-1} for muscle [60].

To ensure efficient photoacoustic signal generation, the laser pulse duration should be on the order of nanoseconds. This duration must be shorter than both the thermal and acoustic confinement times:

$$\tau < \frac{l_c}{v_s} < \frac{l_c^2}{4\alpha_{\,th}}$$

,

where l_c is the characteristic length of heat heterogeneity (the desired spatial resolution), and $\alpha_{\,th}$ is the thermal diffusivity (~0.1 mm^2/s for tissue) [59].

For a short laser pulse, the fractional volume expansion is negligible, and the local pressure rise p immediately after the laser excitation can be derived from (1) as follows [61]:

$$\Delta\, p\,(\vec{r}) = \frac{\beta\, \Delta\, T\,(\vec{r})}{k}$$

The temperature increase can be further described as a function of optical absorption:

$$T = \frac{A_e}{\rho\, C_V}$$

where A_e is the specific or volumetric optical absorption, ρ is the mass density (~1000 kg/m^3 for water and soft tissue), C_V is the specific heat capacity at constant volume (~4000 J/(kg·K) for muscle).

The PA pressure can be written as:

$$p = \frac{\beta}{k\rho\, C_V} A_e = \Gamma A_e$$

,

where Γ is the Grueneisen parameter.

Thus, variation in the optical absorption of the media located on the x-y stage of the experimental set-up (shown in Fig. 2a) leads to a variation of the registered PA response magnitude (as we can see it from the tissue phantom inclusion with different concentrations of GE-NPs on its surface, depicted in Fig. 2b). Tissue phantoms were constructed from agarose gel A9539 (Sigma-Aldrich). To simulate tissue heterogeneity, a density difference was introduced between the spherical-like 5 × 3 mm inclusions and the surrounding phantom matrix by adjusting the concentration of agarose powder in water-based gel for each component (2 wt%.and 1.5 wt%.of powder, respectively). The observed time delay of over 10 microseconds is indicative of the time required

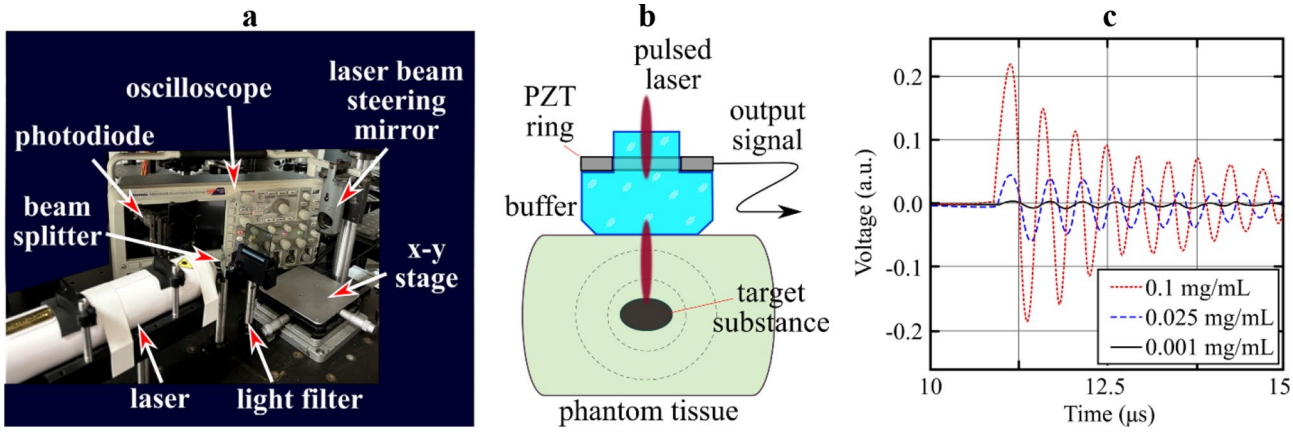

Fig. 2 Typical experimental set-up for photoacoustic measurements (**a**) schematic of tumor phantom and piezoelectric sensor with transparent buffer used (**b**) typical photoacoustic signal for 5 × 3 mm inclusion with different concentrations of GE-NPs inside the tissue phantoms (**c**)

Table 1 The extracellular level of L-[^{14}C]glutamate in nerve terminal preparations

	The extracellular level of L-[^{14}C] glutamate in nerve terminal preparations (% of total accumulated label)	F; *p*-value
Control	30.49 ± 0.79	
GE-NPs ; 0.1 mg/ml	29.68 ± 0.84	$F_{(1,22)} = 0.55$; $p = 0.46$; n.s.
GE-NPs; 0.5 mg/ml	30.18 ± 0.82	$F_{(1,22)} = 0.08$; p = 0.77; n.s.
GE-NPs; 1.0 mg/ml	29.16 ± 0.75	$F_{(1,22)} = 1.63$; $p = 0.21$; n.s.

for acoustic waves to travel from their generation site within the tissue, through the PA glass probe, and reach the detector.

Experiments ex vivo using animals: neurotoxicity risk assessment of GE-NPs

Toxicity risk assessment of GE-NPs was carried out using model of isolated rat brain nerve terminals that allowed analyzing ability of GE-NPs to affect the most complicated nerve signal transduction, and simultaneously examining their membrane tropic activity. Acute neurotoxicity study was done by monitoring key characteristics of glutamatergic neurotransmission. Importantly, impaired transport of the main excitatory neurotransmitter glutamate is involved in the pathogenesis of major neurological and neurodegenerative disorders and diseases. Increased concentration of glutamate in the synaptic cleft over individual threshold leads to neurotoxicity and neuronal death through over- activation of post-synaptic glutamate receptors, and uncontrolled release of Ca^{2+} into the cytoplasm [25, 62, 63].

The extracellular level of L-[^{14}C]glutamate in nerve terminals

The extracellular level of L-[^{14}C]glutamate between episodes of exocytosis is established by a dynamic balance of permanent transporter-mediated release and uptake of L-[^{14}C]glutamate, and also reflects the integrity of the plasma membrane of the presynaptic nerve terminals [64]. As shown in Table 1, the extracellular level of L-[^{14}C]glutamate in the nerve terminal preparations was not changed by GE-NPs at concentrations of 0.1–1.0 mg/ml. Therefore, GE-NPs did not alter dynamic balance of transporter-mediated release and uptake of L-[^{14}C]glutamate, and also GE-NPs had no membrane tropic features, and did not disturb the membrane integrity of the nerve terminals.

Data were analysed using one-way ANOVA. Data are the mean ± SEM., n.s., no significant differences compared to the control; $n = 12$.

Table 2 Depolarization-induced transporter-mediated release of L-[^{14}C]glutamate from nerve terminals

	The transporter-mediated release of L-[^{14}C]glutamate from nerve terminals (% of total accumulated label)	F; *p*-value
Control	13.95 ± 0.54	
GE-NPs ; 0.1 mg/ml	14.18 ± 0.67	$F_{(1,22)} = 0.07$; $p = 0.78$; n.s.
GE-NPs; 0.5 mg/ml	13.74 ± 0.72	$F_{(1,22)} = 0.06$; p = 0.80; n.s.
GE-NPs; 1.0 mg/ml	14.32 ± 0.81	$F_{(1,22)} = 0.15$; $p = 0.70$; n.s.

Data were analysed using one-way ANOVA. Data are the mean ± SEM., n.s., no significant differences compared to the control; $n = 12$

Depolarization-induced transporter-mediated release of L-[^{14}C]glutamate from nerve terminals

Glutamate transporters, membrane proteins, are key players in synaptic neurotransmission, and use Na/K electrochemical gradient across the plasma membrane as driving force. Depolarization-induced transporter-mediated glutamate release to the synaptic cleft (in other terms, glutamate transporter reversal) is the main mechanism for the development of neurotoxicity under conditions of energy supply deficiency, e.g. hypoxic conditions, stroke, brain trauma, etc. Under these pathological conditions, glutamate transporters start to release glutamate to the synaptic cleft [25, 62–64].

GE-NPs at concentrations of 0.1–1.0 mg/ml did not influence synaptosomal transporter-mediated release of L-[^{14}C]glutamate stimulated by 35 mM KCl in Ca^{2+}-free media (Table 2). Therefore, GE-NPs did not increase pathological glutamate transporter reversal, which is the main mechanism for development of glutamate excitotoxicity. This data agreed with the results on the absence of GE-NP effects on the extracellular level of L-[^{14}C]glutamate in nerve terminal preparations presented in Table 1.

Exocytotic release of L-[^{14}C]glutamate from nerve terminals

Stimulated compound exocytosis is the main mechanism of nerve signal transduction. KCl (35 mM) - induced exocytotic release of L-[^{14}C]glutamate from nerve terminals in Ca^{2+}-containing media was not decreased by GE-NPs (Table 3). Therefore, GE-NPs did not affect exocytotic release of L-[^{14}C]glutamate from nerve terminals, and so preserved normal nerve signal transduction.

Transporter-mediated uptake of L-[^{14}C]glutamate by nerve terminals

Removal of excess glutamate from the synaptic cleft after exocytosis, and prevention of neurotoxicity events occur through glutamate uptake by glutamate transporters [25, 62–64]. As shown in Table 4, GE-NPs at concentrations

Table 3 Exocytotic release of L-[^{14}C]glutamate from nerve terminals

	Exocytotic release of L-[^{14}C]glutamate from nerve terminals (% of total accumulated label)	F; *p*-value
Control	5.47 ± 0.74	
GE-NPs ; 0.1 mg/ml	5.22 ± 1.10	$F_{(1,22)} = 0.04$; $p = 0.84$; n.s.
GE-NPs; 0.5 mg/ml	5.82 ± 0.68	$F_{(1,22)} = 0.13$; p = 0.72; n.s.
GE-NPs; 1.0 mg/ml	5.99 ± 0.89	$F_{(1,22)} = 0.22$; $p = 0.64$; n.s.

Data were analysed using one-way ANOVA. Data are the mean ± SEM., n.s., no significant differences compared to the control; $n = 12$

of 0.1–1.0 mg/ml did not change the initial rate of uptake and accumulation of L-[^{14}C]glutamate for 10 min by nerve terminals. These data agreed with all above L-[^{14}C] glutamate results presented in Tables 1, 2 and 3. Therefore, GE-NPs did not affect any key synaptic parameters in nerve terminals, and so they did not have neurotoxic signs and were biocompatible.

Experiments in vivo using animals: anticancer activity of GE-NPs

A highly metastatic Lewis lung carcinoma was used in the experiments. Seek Thermal Imager was used for tumor imaging (Fig. 3).

Tumor growth parameter

In case of multiple subcutaneous injections, GE-NPs-treated LLC-bearing mice had significant tumor growth inhibition at the 14th -18th days of treatment compared to the vehicle group with a maximum inhibition of 77.3% (Day 17). Lung metastases were observed in all vehicle-treated mice, and 1 out of 3 GE-NPs-treated tumor-bearing mice (Fig. 4).

Hematological and serum biochemical parameters

Vehicle-treated tumor-bearing mice demonstrated a significant increase of ASAT, a tendency to increase of GGT and LDH, and a tendency to decrease urea ($p < 0.1$) compared to healthy control, which might be the consequence of liver function alteration (ASAT, GGT) and tumor growth (LDH). GE-NPs-treated mice had significantly decreased LDH compared to vehicle-dosed tumor-bearing animals. This might evidence the probable protection of the liver and attenuating the systemic consequences of tumor growth, as evidenced by the normalization of serum ASAT, and LDH levels (Figs. 5 and 6).

According to hematological analysis, vehicle-treated animals demonstrated a significant increase in white blood cells (WBC), granulocytes (GRAN) count and percentage, mean cell hemoglobin (MCH) and mean cell hemoglobin concentration (MCHC), and decrease of lymphocytes (LYM) percentage, red blood cells (RBC), hemoglobin (HGB), hematocrit (HCT) compared to healthy control. Treatment with GE-NPs caused an increase of RBC and HCT up to the healthy control levels (Figs. 5 and 6).

Photoacoustic therapy of LLC-bearing animals using GE-NPs and irradiation

Figure 7 allows comparison of mouse survival treated in a different way. Intratumoral injection of carbon nanoparticles and subsequent irradiation (during up to 10 min) of the tumors were performed on the 10th day after the tumor introduction. As one can see, combination of the nanoparticle injection and the irradiation of tumors with the laser results in significant increase of mice survival on 54% and 75%, depending on the irradiation time. The more prolonged the radiation – the more increased the survival. It should be noted, that either single GE-NPS injection without irradiation, or irradiation itself (of vehicle-treated mice) did not cause siggnificant changes in mice survival (Table 5). Because the laser-induced localized heating of mice skin has never exceeded 2 °C throughout the entire time of treatment, the main mechanism responsible for the observed therapeutic effect can be related to a photo-acoustically induced destruction of cancer cells significantly enhanced by presence of the incorporated GE-NPs.

Table 4 L-[^{14}C]glutamate uptake by nerve terminals in the presence of GE-NPs

	The initial rate of L-[^{14}C]glutamate uptake by nerve terminals (nmol/min/mg of protein)	F; *p*-value	Accumulation of L-[^{14}C]glutamate by nerve terminals for 10 min (nmol/mg of protein)	F; *p*-value *p*-value
Control	2.43 ± 0.07		9.81 ± 0.14	
GE-NPs 0.1 mg/ml	2.57 ± 0.11	$F_{(1,22)} = 1.21$; p = 0.28; n.s.	9.61 ± 0.18	$F_{(1,22)} = 0.85$; p = 0.36; n.s.
GE-NPs 0.5 mg/ml	2.38 ± 0.08	$F_{(1,22)} = 0.22$; p = 0.64; n.s.	9.94 ± 0.17	$F_{(1,22)} = 0.40$; p = 0.53; n.s.
GE-NPs 1.0 mg/ml	2.28 ± 0.14	$F_{(1,22)} = 0.95$; p = 0.33; n.s.	9.53 ± 0.23	$F_{(1,22)} = 1.16$; p = 0.29; n.s.

Data were analysed using one-way ANOVA. Data are the mean ± SEM., n.s., no significant differences compared to the appropriate control; $n = 12$

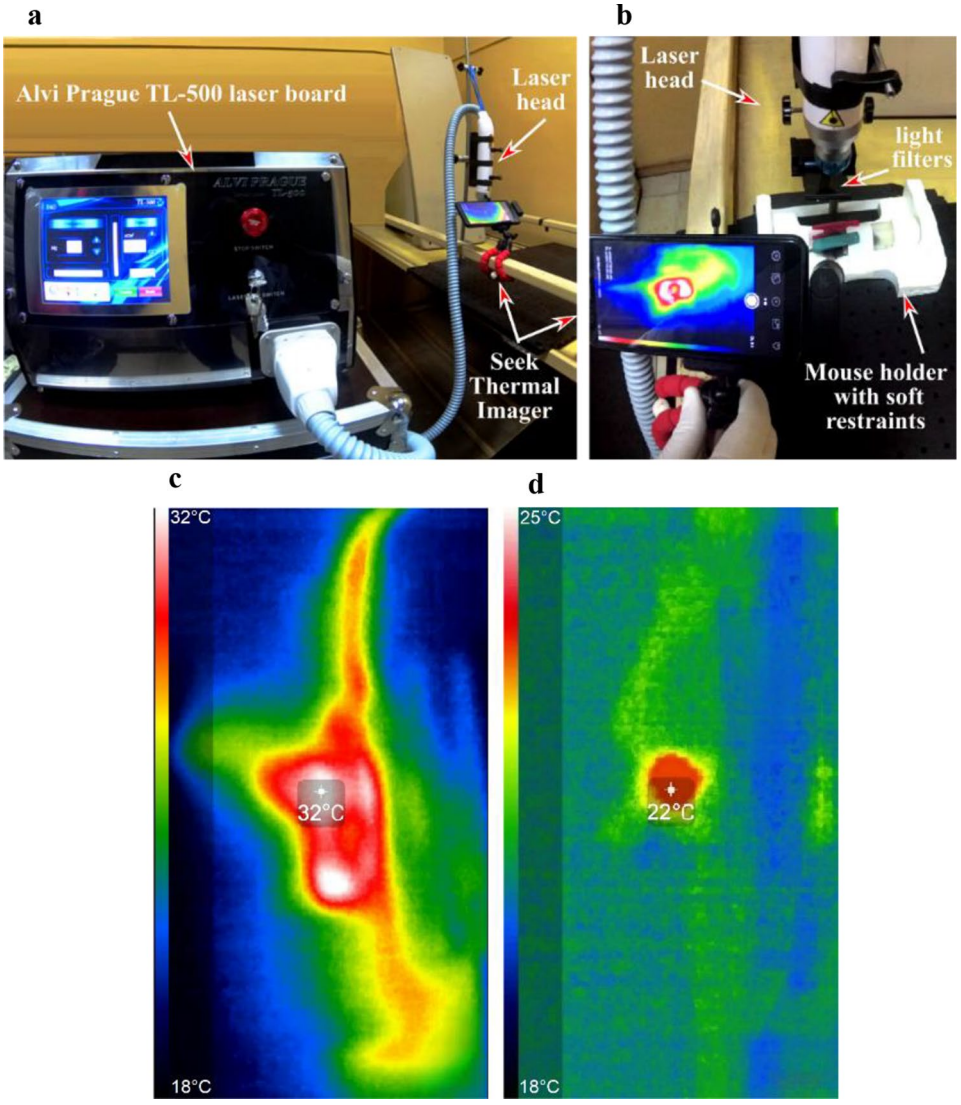

Fig. 3 Experimental set-up for mice irradiating (**a**, **b**), typical image of laser beam spot on tumor site of alive (**c**) and died (**d**) LLC-bearing mouse obtained using Seek Thermal imager

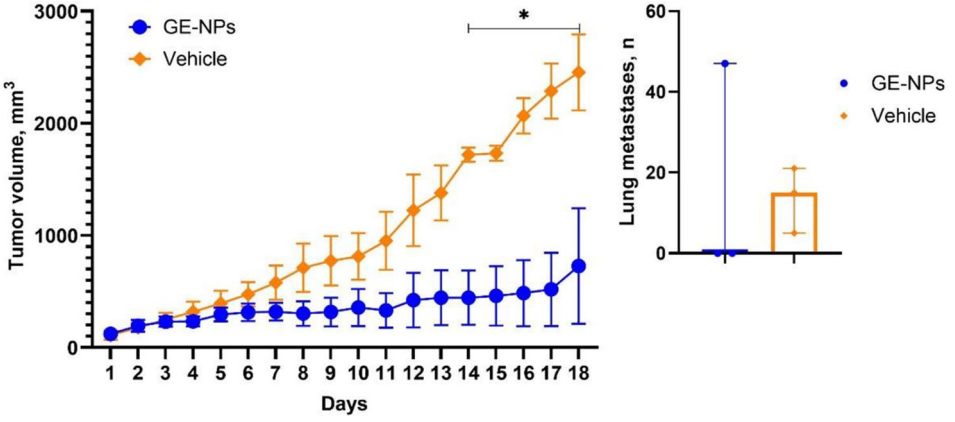

Fig. 4 The dynamics of tumor growth and lung metastases count in LLC-bearing mice after treatment with GE-NPs

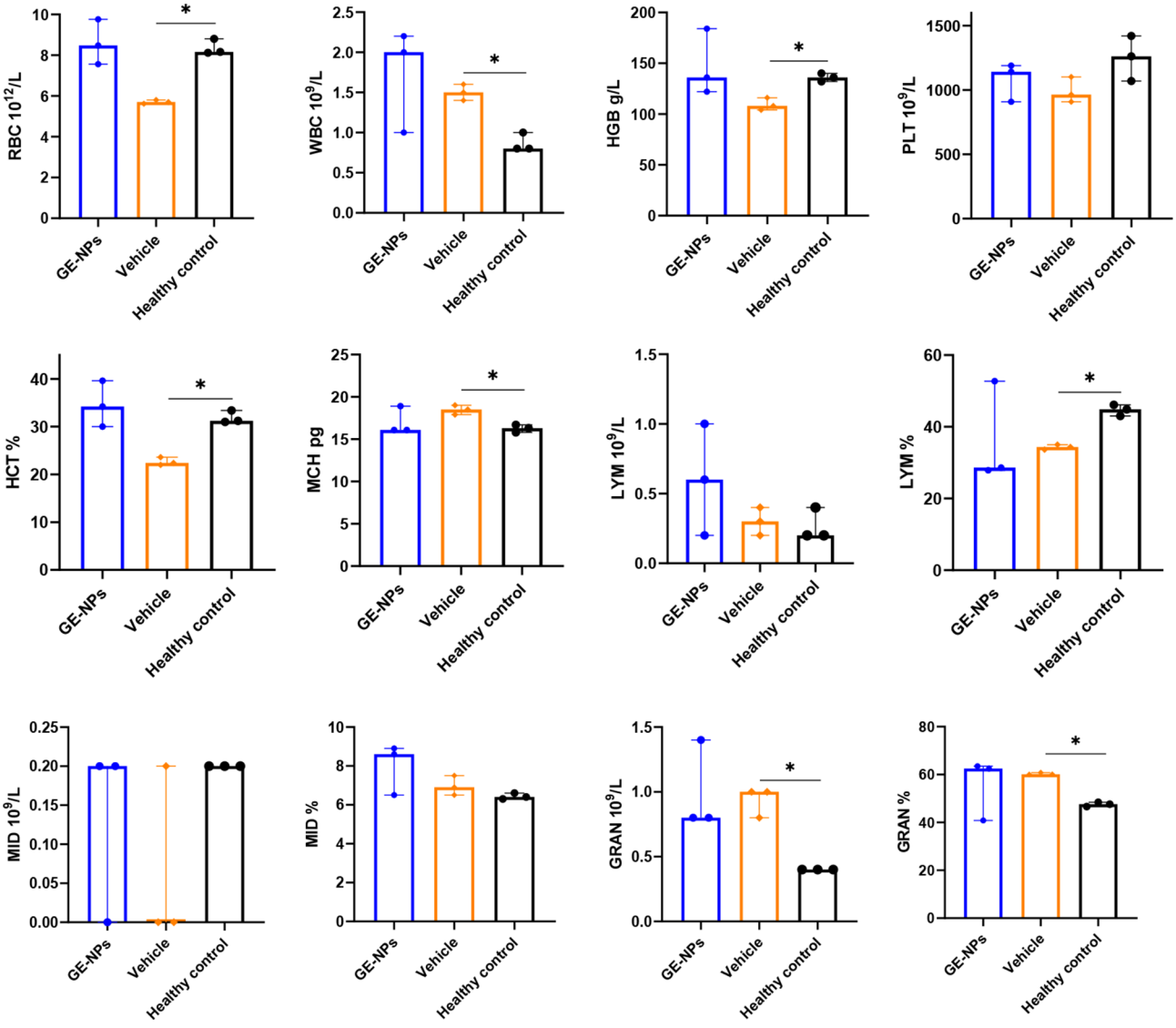

Fig. 5 Hematological parameters of LLC-bearing mice after vehicle or GE-NPs treatment compared to healthy control

To analyse the effect shown in Fig. 8 in details, the following experiments were done involving different combinations of influenced factors and parameters.

As shown in Fig.8, the tumor volume increased linearly up to the 25th day post-inoculation. This trend continued for the Vehicle-treated mice, both irradiated and non-irradiated, up to their death. However, mice treated with GE-NPs followed by irradiation exhibited a stable tumor volume, reaching a plateau up to the end of the study. Notably, GE-NPs-treated mice without irradiation also reached a tumor volume plateau, albeit later, around the 30th day post-inoculation. Although there was no significant difference in tumor volume between the groups, the stabilization of tumor growth, combined with a significant increase in survival, suggests a substantial enhancement of the antitumor effect of GE-NPs by irradiation. Additionally, the duration of irradiation correlates with smaller stabilized tumor volumes (Fig. 8).

It should be noted, however, that further increase of irradiation time to 20 min led to mouse heating and reducing of mice survival (data not shown).

Discussion

Literature data analysis has shown that the photoacoustic approach was used mainly for imaging. Photoacoustic tomography is a non-invasive/non-ionizing imaging technique that combines optical specificity and sensitivity with high resolution and penetration depth of ultrasound [47], and it remains one of the perspective techniques for theranostic applications in humans [65]. Photoacoustic imaging uses light as an excitation source and ultrasound detector to monitor sound waves generated by the optically-excited targets [66]. Optical photons

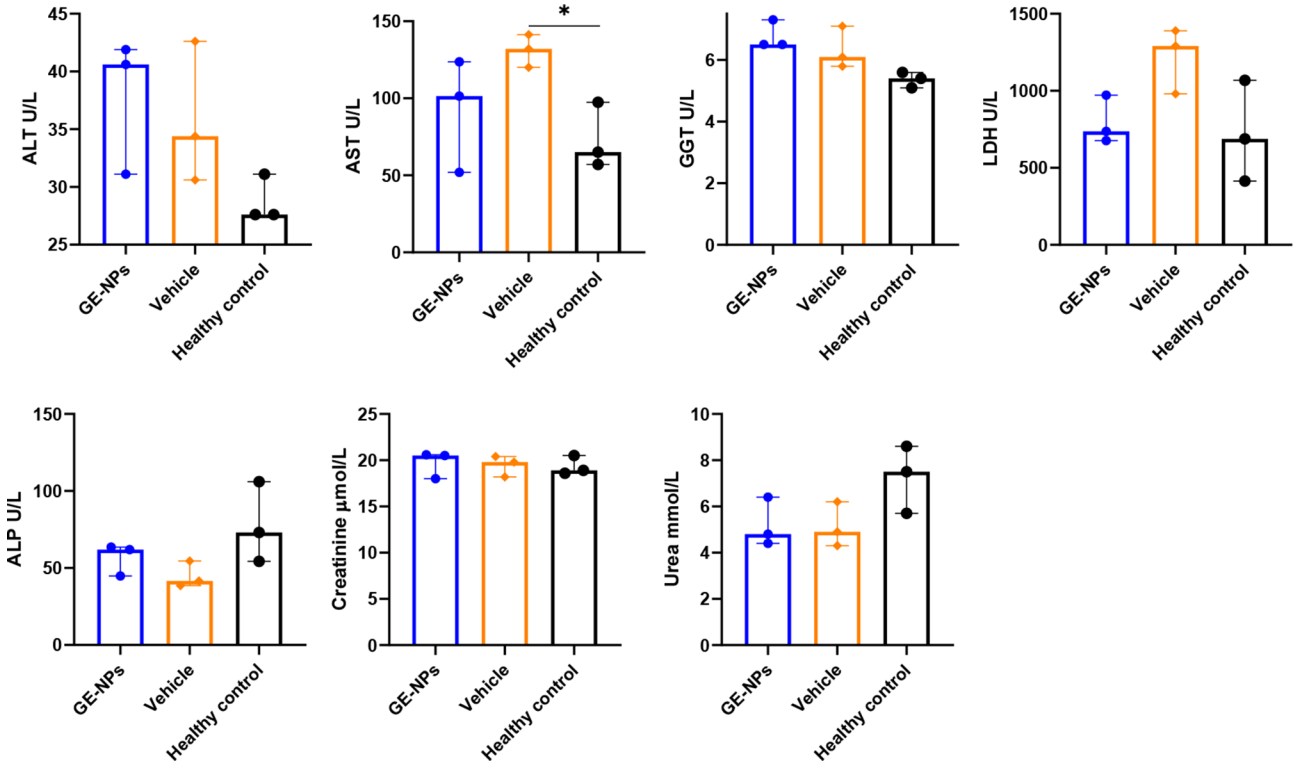

Fig. 6 Biochemical parameters of LLC-bearing mice after vehicle or GE-NPs treatment compared to healthy control

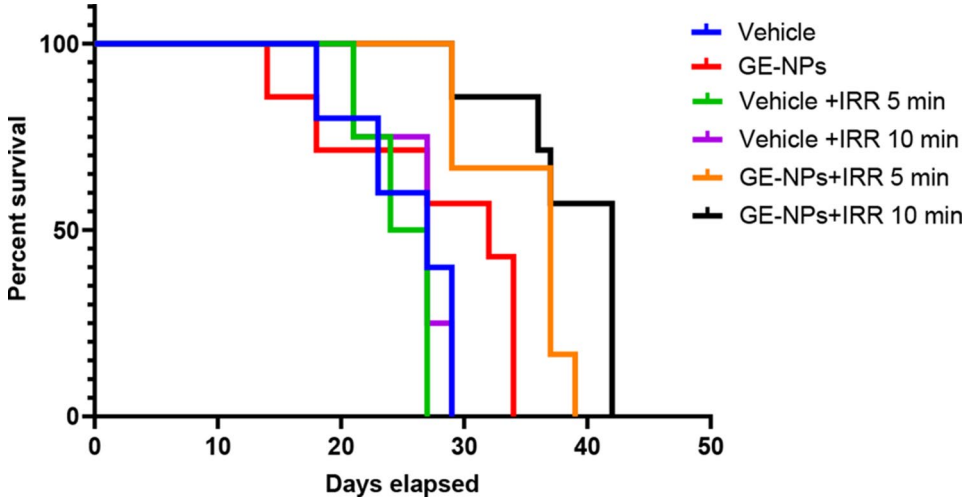

Fig. 7 Mice survival for animals treated with Vehicle or GE-NPs and irradiated with nanosecond pulse laser for 5 and 10 min. Medians of survival and the significances of the difference are shown in Table 5

are absorbed and converted to heat; the transient thermoelastic expansions of heated biological tissues lead to the emission of acoustic waves [67]. It is an emerging modality for molecular imaging of cancer and preclinical studies using mouse models have demonstrated perspectives in the assessment of response to radiotherapy and chemoradiotherapy [68]. The photoacoustic signal can be significantly amplified by using contrast agents. A potential contrast material for photoacoustic imaging should possess both features, namely, high photon absorbance and sufficient conversion efficiency from light to heat [67]. Carbon nanomaterials are perfect candidates for photoacoustic imaging due to their superior absorption coefficients in the near-infrared spectral region, making them perfect among a wide variety of exogenous contrast agents [67, 69].

In this study, our primary focus was to evaluate the capacity of GE-NPs, which had previously shown

Table 5 Medians of survival of mice treated with single intratumoral injection of vehicle or GE-NPs and irradiated (IRR) with nanosecond pulse laser (1064 and 532 nm wavelengths and 1 hz of pulse repetition rate) for 5 and 10 min

	Medians (95% CI)	*p*-value
Vehicle, $n=5$	27 (18.4–35.6)	$p=0.849$; n.s.
GE-NPs, $n=7$	32 (19.2–44.8)	
Vehicle + IRR 5 min, $n=4$	25.5 (20.1–27.9)	$p=0.028$
GE-NPs + IRR 5 min, $n=6$	37 (32.2–41.8)	
Vehicle + IRR 10 min, $n=4$	24 (18.1–29.9)	$p=0.002$
GE-NPs + IRR 10 min, $n=7$	42 (34.9–42.3)	

efficiency in photoacoustic imaging, to be effective in photoacoustic therapy, which in turn should be biocompatible for further successful medical implementation.

Here, it was demonstrated that GE-NPs within the concentration range 0.1–1 mg/ml demonstrated low neurotoxicity ex vivo when measuring the extracellular level, transporter-mediated and exocytotic release and uptake of the excitatory neurotransmitter L-[^{14}C]glutamate in nerve terminals (Tables 1, 2, 3 and 4). Previous results on neurotoxicity risk assessment of CDs [25, 62] allow us to compare neuroactive properties of different nanoparticles. In particular, GE-NPs at a concentration 1 mg/ml did not change the extracellular level, transporter-mediated and exocytotic release and uptake of L-[^{14}C]glutamate in nerve terminals (Tables 1, 2, 3 and 4), whereas CDs synthesized from β-alanine decreased the exocytotic release and uptake of L-[^{14}C]glutamate in nerve terminals starting from the concentration of 0.08 mg/ml and increased the extracellular level of L-[^{14}C]glutamate starting from 0.2 mg/ml. CDs derived from the sulfur-containing precursor thiourea decreased L-[^{14}C]glutamate uptake by nerve terminals and increased its extracellular level at a concentration of 0.5 mg/ml. As a result, GE-NPs exhibit lower neurotoxicity signs compared to the above-mentioned CDs. These data agreed with our previous results, where a human lung cancer A549 cells were used for cytotoxicity study of GE-NPs [21]. In particular, toxicity assessment using A549 cells after 24 h of incubation showed no changes in cell viability and morphology at concentrations of 1.5 mg/ml and lower. If applied at the highest concentration (2.0 mg/mL), GE-NPs demonstrated cytostatic activity (cell growth inhibiting) [21]. However, despite no neurotoxicity ex vivo being revealed for GE-NPs even at a high concentration, in vivo experiments using animals are required to prove their biocompatibility and biosafety.

Data on low toxicity ex vivo agreed with our previous results, where GE-NPs were administrated in vivo in Wistar rats without visible health consequences [48]. In another study, the in vivo toxicity of GE-NPs was comprehensively assessed using a mouse model. It was shown that GE-NPs did not affect C57Bl6 mice wellbeing after multiple dosages (5 mg/kg subcutaneously) for 14 days. Comparative analysis of CDs with different surface properties revealed that CDs with surface carboxyl and phenol groups accompanied by nitrogen and trifluoromethyl groups, were the most impactful for all organs [21].

In this study, the efficiency of cancer treatment by GE-NPs was proven in vivo experiments using mice bearing Lewis lung carcinoma after inoculation (Figs. 7 and 8). Mice daily treated with GE-NPs during 18 days demonstrated significant tumor growth inhibition at the 14th -18th days of treatment as compared to vehicle group with maximum inhibition by 77.3% (Day 17), while those treated once had no difference in tumor volume compared to vehicle group. Notably, GE-NPs daily injections significantly inhibited tumor growth, stabilizing the tumor volume almost at the initial level, probably because of the impact on every tumor cell generation. While single GE-NP administration followed by irradiation stabilized the tumor volume as well, but after some period of time and after achieving some tumor volume.

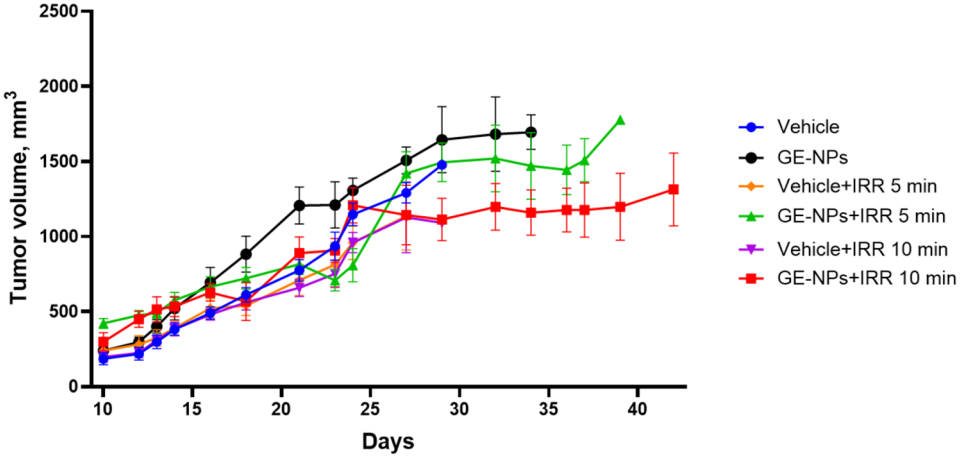

Fig. 8 The dynamics of tumor growth in LLC-bearing mice after single administration of GE-NPs accompanied with irradiation

This might happen because of the different mechanisms of action of GE-NP itself and after activation with irradiation. Additionally, it is worth noting, that the tumors in the Vehicle-treated group in the "irradiation" study did not reach 2000 mm^3 even 30 days post-dosing, compared to 2500 mm^3 on the 18th day of the treatment in "no irradiation" study. Thus, while tumor growth reduction in the "irradiation" study may not appear dramatic, survival benefits are likely attributable to effects on tumor biology and metastasis inhibition.

In preclinical studies, tumor growth inhibition without full eradication can still hold significant clinical relevance for several reasons, as delayed disease progression, improved survival (as we observed in our study), therapeutic window for treatment combinations like immunotherapy, chemotherapy, or radiation therapy, symptom management and quality of life, sometimes, tumor dormancy and immune control. Therefore, demonstrating tumor growth inhibition in preclinical models better mirrors the partial responses seen in clinical settings, making such models highly valuable for predicting clinical responses and optimizing treatment strategies. Importantly, our previous study has demonstrated the potential effectiveness of GE-NPs for photoacoustic imaging, and their prospects for various photoacoustic approaches have been predicted [48]. In particular, bio-distribution of GE-NPs after 24 h of their intravenous injection was investigated using a photoacoustic approach. A 16 ns light pulse from a Q-switched Nd: YAG laser with 1064 nm wavelength was used as the excitation source, and the laser-induced photoacoustic signals were captured with a ring piezoelectric detector. It was shown that the GE-NPs were mainly found in the liver, kidneys and spleen, with lower accumulation in the heart and gastrocnemius muscles. It was concluded in this study that among other studied carbon NPs, i.e. carbon nanodots from urea-citric acid, β-alanine, and carbon furooxide nanoparticles, GE-NPs were the most promising. It was clearly stated that increasing photoacoustic signals in the brain after administration of GE-NPs can be used as a potential model for detailed investigation of blood-brain barrier permeability. The high amplitude of photoacoustic signals and the high capability of GE-NPs to convert absorbed light into heat compared to other carbon NPs make GE-NPs perspective agents for photothermal approaches. In this context, GE-NPs can be recommended not only for photoacoustic imaging but also for photothermal therapy of cancer [48].

The main finding of this study is the fact that efficacy of GE-NPs for photoacoustic therapy has been demonstrated in vivo using mice subcutaneously grafted with Lewis lung carcinoma cells. In particular, the combined application of intratumoral injection of GE-NPs and irradiation by the laser beam during 5 and 10 min resulted in an increase in mice survival on more than 30% compared to GE-NPs-treated non-irradiated mice, and up to 75% depending on the irradiation duration, and a tumor volume stabilization, as it was not reduced but stopped to growth after 25 days post-inoculation. The observed therapeutic effect can be related to the photoacoustically-induced destruction of cancer cells, and significantly enhanced by the presence of the incorporated GE-NPs because the laser-induced localized heating of mice skin has never exceeded 2 °C during the entire time of treatment. Therefore, efficiency of photoacoustic therapy for carcinoma in mice using biocompatible GE-NPs was demonstrated for the first time, showing potential for medical application. It should be noted that an increase in irradiation time to 10 and 20 min led to more complicated dependencies, in particular, 20 min irradiation resulted in mouse heating and reducing of mice survival.

Conventional lung cancer treatments primarily involve chemical-based approaches, such as chemotherapy, immunotherapy, and targeted therapies, which aim to destroy cancer cells. However, these treatments often impact non-cancerous cells due to the challenge in achieving absolute selectivity, leading to notable side effects. Radiotherapy, which uses targeted heat to damage tumors, also faces limitations in precision, risking damage to surrounding healthy tissues. Photothermal therapy (PTT) offers a combination of these two approaches' advantages: it uses the specificity of chemical agents to target cancer cells, coupled with the destructive power of a laser beam to selectively kill cancer cells. This dual-action allows for a reduction in the "dose" of each component, maintaining effectiveness while minimizing side effects.

For example, combining PTT with chemotherapy, such as with gold nanorods and doxorubicin, has shown enhanced efficacy, achieving up to 11 times greater effectiveness than either treatment alone [70]. Additionally, many PTT agents, like polyethylene glycol-modified polymers, exhibit excellent biocompatibility, reducing adverse effects compared to traditional chemotherapies [71] Furthermore, PTT enables localized hyperthermia, which induces ROS generation to enhance cancer cell apoptosis while sparing healthy cells [72]. Real-time monitoring techniques like photoacoustic imaging also facilitate treatment adjustments during therapy, increasing overall efficacy [71] as well.

The long-term circulating time of GE-NPs in the organism shown in our previous study [48] favours potential GE-NPs accumulation by tumor due to passive targeting and enhanced permeation and retention effect, that makes GE-NPs not only perspective agents in photoacoustic therapy after intratumoral application shown in this study, but also for photoacoustic therapy using intravenous administration.

Conclusions

Summarizing, this study aims to prove the effectiveness of highly biocompatible GE-NPs for photoacoustic therapy. The photoacoustic imaging potential of these NPs has been demonstrated in a previous study [48]. Injection of GE-NPs into mouse tumor and irradiation by laser beam resulted in an increase in mice survival and a decrease in the growth rate of the cancerous tumor. The observed therapeutic effect may result from a photoacoustically induced destruction of cancer cells enhanced by injected GE-NPs. Therefore, GE-NPs possess dual potential in cancer theranostics for both photoacoustic imaging and therapy by applying different irradiation conditions.

Acknowledgements

This research was funded by the European Commission, Program H2020-MSCA-RISE-2015, Project N°690945 "Carther" (2016–2019); EU Horizon 2020 Research and Innovation Staff Exchange Programme (RISE) under Marie Skłodowska-Curie Action (project 101008159 "UNAT") (2021–2026); photoacoustic study was supported by Ministry of Education and Science of Ukraine under Grant No. 0124U001084 (PI: P. Lishchuk); neurotoxicity study was funded by the National Research Foundation of Ukraine: NRFU grant # 2021.01/0061 «Cumulative neurotoxic effect of multicomponent pollution by airborne particles and neuroactive pharmaceuticals, biomaterials (including SARS-CoV-2), toxic metals and its prevention» (PI: T. Borisova).

Author contributions

GE-NPs synthesis and characterization– SA; photoacoustic measurements - PL, MI, VL; cytotoxicity study – AP; rat brain synaptosome preparations were obtained by AP, L-[14 C] glutamate experiments – AP, KN; experiments in vivo using mice – HK, ND, LG, TD; data analysis and figure preparation – NP, KN, VL, VS, HK, LG, TB; experimental design, funding acquisitions, project leading – VL, VS; data analysis and paper writing – VL, VS, HK,TB. All authors read and approved the final manuscript.

Data availability

No datasets were generated or analysed during the current study.

Declarations

Competing interests

The authors declare no competing interests.

Author details

[1]Taras Shevchenko National University of Kyiv, 64/13, Volodymyrska Street, Kyiv 01601, Ukraine
[2]Corporation Science Park Kyiv, Taras Shevchenko University, 60, Volodymyrska Street, Kyiv 01033, Ukraine
[3]Université de Lorraine, CNRS, LEMTA, Nancy F-54000, France
[4]Palladin Institute of Biochemistry, National Academy of Sciences of Ukraine, 9 Leontovicha Street, Kiev 01054, Ukraine
[5]Light Matter Institute, UMR-5306, Claude Bernard University of Lyon/CNRS, Université de Lyon, Villeurbanne Cedex 69622, France

Received: 4 September 2024 / Accepted: 26 December 2024
Published online: 08 January 2025

References

1. WHO. (2024) Global cancer burden growing, amidst mounting need for services. https://www.who.int/news/item/01-02-2024-global-cancer-burden-growing--amidst-mounting-need-for-services. Accessed 18 Jul 2024.
2. Riehemann K, Schneider SW, Luger TA, et al. Nanomedicine—Challenge and perspectives. Angew Chem Int Ed. 2009;48:872–97. https://doi.org/10.1002/anie.200802585.
3. Raj R, Mongia P, Kumar Sahu S, Ram A. Nanocarriers Based Anticancer drugs: current scenario and future perceptions. Curr Drug Targets. 2016;17:206–28. https://doi.org/10.2174/1389450116666150722141607.
4. Cho H-S, Dong Z, Pauletti GM, et al. Fluorescent, superparamagnetic nanospheres for drug Storage, Targeting, and imaging: a multifunctional Nanocarrier System for Cancer diagnosis and treatment. ACS Nano. 2010;4:5398–404. https://doi.org/10.1021/nn101000e.
5. Yuan Y, Guo B, Hao L, et al. Doxorubicin-loaded environmentally friendly carbon dots as a novel drug delivery system for nucleus targeted cancer therapy. Colloids Surf B Biointerfaces. 2017;159:349–59. https://doi.org/10.1016/j.colsurfb.2017.07.030.
6. Kumar PSR. Nanomedicine for cancer therapy: from chemotherapeutic to hyperthermia-based therapy. Springer; 2017.
7. Hussen NH, Hasan AH, FaqiKhedr YM, et al. Carbon dot based Carbon nanoparticles as Potent Antimicrobial, Antiviral, and Anticancer agents. ACS Omega. 2024;9:9849–64. https://doi.org/10.1021/acsomega.3c05537.
8. Garcia-Prada CD, Carmes L, Atis S, et al. Gadolinium-based nanoparticles sensitize ovarian peritoneal carcinomatosis to targeted Radionuclide Therapy. J Nucl Med. 2023;64:1956–64. https://doi.org/10.2967/jnumed.123.265418.
9. Shen C-L, Liu H-R, Lou Q, et al. Recent progress of carbon dots in targeted bioimaging and cancer therapy. Theranostics. 2022;12:2860–93. https://doi.org/10.7150/thno.70721.
10. Bhattacharya T, Preetam S, Mukherjee S, et al. Anticancer activity of quantum size carbon dots: opportunities and challenges. Discover Nano. 2024;19:122. https://doi.org/10.1186/s11671-024-04069-7.
11. Kim GJ, Nie S. Targeted cancer nanotherapy. Mater Today. 2005;8:28–33. https://doi.org/10.1016/S1369-7021(05)71034-8.
12. Peer D, Karp JM, Hong S, et al. Nanocarriers as an emerging platform for cancer therapy. Nat Nanotechnol. 2007;2:751–60. https://doi.org/10.1038/nnano.2007.387.
13. Yu MK, Park J, Jon S. Targeting strategies for multifunctional nanoparticles in Cancer Imaging and Therapy. Theranostics. 2012;2:3–44. https://doi.org/10.7150/thno.3463.
14. Naik K, Chaudhary S, Ye L, Parmar AS. A Strategic Review on Carbon Quantum dots for Cancer-Diagnostics and Treatment. Front Bioeng Biotechnol. 2022;10. https://doi.org/10.3389/fbioe.2022.882100.
15. Ku T-H, Shen W-T, Hsieh C-T, et al. Specific Forms of Graphene Quantum dots induce apoptosis and cell cycle arrest in breast Cancer cells. Int J Mol Sci. 2023;24:4046. https://doi.org/10.3390/ijms24044046.
16. Iannazzo D, Ziccarelli I, Pistone A. Graphene quantum dots: multifunctional nanoplatforms for anticancer therapy. J Mater Chem B. 2017;5:6471–89. https://doi.org/10.1039/c7tb00747g.
17. Ghosh D, Sarkar K, Devi P, et al. Current and future perspectives of carbon and graphene quantum dots: from synthesis to strategy for building optoelectronic and energy devices. Renew Sustain Energy Rev. 2021;135:110391. https://doi.org/10.1016/j.rser.2020.110391.
18. Wang Y, Wang H, Liu D, et al. Graphene oxide covalently grafted upconversion nanoparticles for combined NIR mediated imaging and photothermal/photodynamic cancer therapy. Biomaterials. 2013;34:7715–24. https://doi.org/10.1016/j.biomaterials.2013.06.045.
19. Yang C, Chan KK, Xu G, et al. Biodegradable polymer-coated multifunctional Graphene Quantum dots for Light-Triggered Synergetic Therapy of Pancreatic Cancer. ACS Appl Mater Interfaces. 2019;11:2768–81. https://doi.org/10.1021/acsami.8b16168.
20. Mohammed S. Graphene oxide: a mini-review on the versatility and challenges as a membrane material for solvent-based separation. Chem Eng J Adv. 2022;12:100392. https://doi.org/10.1016/j.ceja.2022.100392.
21. Kuznietsova H, Géloën A, Dziubenko N, et al. In vitro and in vivo toxicity of carbon dots with different chemical compositions. Discover Nano. 2023;18:111. https://doi.org/10.1186/s11671-023-03891-9.
22. Kuznietsova H, Dziubenko N, Paliienko K, et al. A comparative multi-level toxicity assessment of carbon-based Gd-free dots and Gd-doped nanohybrids from coffee waste: hematology, biochemistry, histopathology and neurobiology study. Sci Rep. 2023;13:9306. https://doi.org/10.1038/s41598-023-36496-4.
23. Jia Q, Zhao Z, Liang K, et al. Recent advances and prospects of carbon dots in cancer nanotheranostics. Mater Chem Front. 2020;4:449–71. https://doi.org/10.1039/c9qm00667b.

24. Zhylkybayeva N, Paliienko K, Topchylo A, et al. Size dependent properties of Gd3+-free versus Gd3+-doped carbon dots for bioimaging application. Sci Rep. 2024;14:27812. https://doi.org/10.1038/s41598-024-76500-z.
25. Borisova T, Nazarova A, Dekaliuk M, et al. Neuromodulatory properties of fluorescent carbon dots: Effect on exocytotic release, uptake and ambient level of glutamate and GABA in brain nerve terminals. Int J Biochem Cell Biol. 2015;59:203–15. https://doi.org/10.1016/j.biocel.2014.11.016.
26. Qu D, Wang X, Bao Y, Sun Z. Recent advance of carbon dots in bio-related applications. JPhys Mater. 2020;3:022003. https://doi.org/10.1088/2515-7639/ab7cb9.
27. Mehra NK, Palakurthi S. Interactions between carbon nanotubes and bioactives: a drug delivery perspective. Drug Discov Today. 2016;21:585–97. https://doi.org/10.1016/j.drudis.2015.11.011.
28. Son KH, Hong JH, Lee JW. Carbon nanotubes as cancer therapeutic carriers and mediators. Int J Nanomed. 2016;11:5163–85. https://doi.org/10.2147/IJN.S112660.
29. Zhang Y, Petibone D, Xu Y, et al. Toxicity and efficacy of carbon nanotubes and graphene: the utility of carbon-based nanoparticles in nanomedicine. Drug Metab Rev. 2014;46:232–46. https://doi.org/10.3109/03602532.2014.883406.
30. Kim D, Jo G, Chae Y, et al. Bioinspired *Camellia japonica* carbon dots with high near-infrared absorbance for efficient photothermal cancer therapy. Nanoscale. 2021;13:14426–34. https://doi.org/10.1039/D1NR03999G.
31. Casais-Molina ML, Cab C, Canto G, et al. Carbon nanomaterials for breast Cancer Treatment. J Nanomater. 2018;2018:1–9. https://doi.org/10.1155/2018/2058613.
32. Dolmans D, Fukumura D, Jain RK. Photodynamic therapy for cancer. Nat Rev Cancer. 2003;3:380–7. https://doi.org/10.1038/nrc1071.
33. Pang W, Jiang P, Ding S, et al. Nucleolus-targeted photodynamic anticancer therapy using renal-clearable Carbon dots. Adv Healthc Mater. 2020;9:e2000607. https://doi.org/10.1002/adhm.202000607.
34. Li X, Vinothini K, Ramesh T, et al. Combined photodynamic-chemotherapy investigation of cancer cells using carbon quantum dot-based drug carrier system. Drug Deliv. 2020;27:791–804. https://doi.org/10.1080/10717544.2020.1765431.
35. Feng S, Lu J, Wang K, et al. Advances in smart mesoporous carbon nanoplatforms for photothermal–enhanced synergistic cancer therapy. Chem Eng J. 2022;435:134886. https://doi.org/10.1016/j.cej.2022.134886.
36. Beik J, Abed Z, Ghoreishi FS, et al. Nanotechnology in hyperthermia cancer therapy: from fundamental principles to advanced applications. J Controlled Release. 2016;235:205–21. https://doi.org/10.1016/j.jconrel.2016.05.062.
37. Wang Z, Yang F, Cheng Z, et al. Photoacoustic-guided photothermal therapy by mapping of tumor microvasculature and nanoparticle. Nanophotonics. 2021;10:3359–68. https://doi.org/10.1515/nanoph-2021-0198.
38. Hester SC, Kuriakose M, Nguyen CD, Mallidi S. Role of Ultrasound and Photoacoustic Imaging in Photodynamic Therapy for Cancer. Photochem Photobiol. 2020;96:260–79. https://doi.org/10.1111/php.13217.
39. Petrovic LZ, Xavierselvan M, Kuriakose M, et al. Mutual impact of clinically translatable near-infrared dyes on photoacoustic image contrast and in vitro photodynamic therapy efficacy. J Biomed Opt. 2020;25:1. https://doi.org/10.1117/1.JBO.25.6.063808.
40. Thanou M, Gedroyc W. MRI-Guided focused Ultrasound as a New Method of Drug Delivery. J Drug Deliv. 2013;2013:1–12. https://doi.org/10.1155/2013/616197.
41. Han X, Huang J, Jing X, et al. Oxygen-deficient black titania for Synergistic/Enhanced Sonodynamic and Photoinduced Cancer Therapy at Near Infrared-II Biowindow. ACS Nano. 2018;12:4545–55. https://doi.org/10.1021/acsnano.8b00899.
42. He Y, Wan J, Yang Y, et al. Multifunctional polypyrrole-coated Mesoporous TiO2 nanocomposites for Photothermal, Sonodynamic, and chemotherapeutic treatments and Dual-Modal Ultrasound/Photoacoustic Imaging of Tumors. Adv Healthc Mater. 2019;8:e1801254. https://doi.org/10.1002/adhm.201801254.
43. Zhang H, Chen J, Zhu X, et al. Ultrasound induced phase-transition and invisible nanobomb for imaging-guided tumor sonodynamic therapy. J Mater Chem B. 2018;6:6108–21. https://doi.org/10.1039/C8TB01788C.
44. Gong F, Cheng L, Yang N, et al. Ultrasmall Oxygen-Deficient Bimetallic Oxide MnWOX nanoparticles for Depletion of endogenous GSH and enhanced Sonodynamic Cancer Therapy. Adv Mater. 2019;31:e1900730. https://doi.org/10.1002/adma.201900730.
45. Wang X, Cheng L. Multifunctional two-dimensional nanocomposites for photothermal-based combined cancer therapy. Nanoscale. 2019;11:15685–708. https://doi.org/10.1039/c9nr04044g.
46. Hola K, Zhang Y, Wang Y, et al. Carbon dots - emerging light emitters for bioimaging, cancer therapy and optoelectronics. Nano Today. 2014;9:590–603. https://doi.org/10.1016/j.nantod.2014.09.004.
47. Xu M, Wang LV. Photoacoustic imaging in biomedicine. Rev Sci Instrum. 2006;77:041101. https://doi.org/10.1063/1.2195024.
48. Dubyk K, Borisova T, Paliienko K, et al. Bio-distribution of Carbon nanoparticles studied by photoacoustic measurements. Nanoscale Res Lett. 2022;17:127. https://doi.org/10.1186/s11671-022-03768-3.
49. Dong W, Zhou S, Dong Y, et al. The preparation of ethylenediamine-modified fluorescent carbon dots and their use in imaging of cells. Luminescence. 2015;30:867–71. https://doi.org/10.1002/bio.2834.
50. Kilkenny C, Browne W, Cuthill IC, et al. Animal research: reporting in vivo experiments: the ARRIVE guidelines. Br J Pharmacol. 2010;160:1577–9. https://doi.org/10.1111/j.1476-5381.2010.00872.x.
51. McGrath JC, Drummond GB, McLachlan EM, et al. Guidelines for reporting experiments involving animals: the ARRIVE guidelines. Br J Pharmacol. 2010;160:1573–6. https://doi.org/10.1111/j.1476-5381.2010.00873.x.
52. Cotman CW. Isolation of synaptosomal and synaptic plasma membrane fractions. Methods Enzymol. 1974;31:445–52.
53. Borisova T. The neurotoxic effects of heavy metals: alterations in acidification of synaptic vesicles and glutamate transport in brain nerve terminals. Horizons Neurosci Res. 2014;14:89–112.
54. Borysov A, Krisanova N, Chunihin O, et al. A comparative study of neurotoxic potential of synthesized polysaccharide-coated and native ferritin-based magnetic nanoparticles. Croat Med J. 2014;55:195–205. https://doi.org/10.3325/cmj.2014.55.195.
55. Larson E, Howlett B, Jagendorf A. Artificial reductant enhancement of the Lowry method for protein determination. Anal Biochem. 1986;155:243–8.
56. (2002) Institutional Animal Care and Use Committee Guidebook.
57. van Fentener JM, Borrens M, Girod A, et al. The reporting of clinical signs in laboratory animals: FELASA Working Group Report. Lab Anim. 2015;49:267–83. https://doi.org/10.1177/0023677215584249.
58. OECD Guidance Document. (2020) Guidance Document on the Recognition, Assessment and Use of Clinical Signs as Human Endpoints for Experimental Animals Used in Safety Evaluation N°19. In: ENV/JM/MONO (2000)7. https://read.oecd-ilibrary.org/environment/guidance-document-on-the-recognition-assessment-and-use-of-clinical-signs-as-human-endpoints-for-experimental-animals-used-in-safety-evaluation_9789264078376-en#page1. Accessed 18 Jul 2024.
59. Xia J, Yao J, Wang LV. Photoacoustic tomography: principles and advances. Progress Electromagnet Res. 2014;147:1–22. https://doi.org/10.2528/PIER14032303.
60. Wang LV. Tutorial on photoacoustic microscopy and computed tomography. IEEE J Sel Top Quantum Electron. 2008;14:171–9. https://doi.org/10.1109/JSTQE.2007.913398.
61. Gusev VE, Karabutov AA. (1993) Laser Optoacoustics. American Institute of Physics. Woodbury, NY, https://www.biblio.com/9781563960369
62. Borisova T, Dekaliuk M, Pozdnyakova N, et al. Harmful impact on presynaptic glutamate and GABA transport by carbon dots synthesized from sulfur-containing carbohydrate precursor. Environ Sci Pollut Res. 2017;24:17688–700. https://doi.org/10.1007/s11356-017-9414-6.
63. Shatursky OYa, Demchenko AP, Panas I, et al. The ability of carbon nanoparticles to increase transmembrane current of cations coincides with impaired synaptic neurotransmission. Biochim et Biophys Acta (BBA) - Biomembr. 2022;1864:183817. https://doi.org/10.1016/j.bbamem.2021.183817.
64. Borisova T. Permanent dynamic transporter-mediated turnover of glutamate across the plasma membrane of presynaptic nerve terminals: arguments in favor and against. Rev Neurosci. 2016;27:71–81. https://doi.org/10.1515/revneuro-2015-0023.
65. Maturi M, Locatelli E, Monaco I, Comes Franchini M. Current concepts in nanostructured contrast media development for: in vivo photoacoustic imaging. Biomater Sci. 2019;7:1746–75. https://doi.org/10.1039/c8bm01444b.
66. Chen YS, Yeager D, Emelianov SY. Photoacoustic imaging for Cancer diagnosis and Therapy Guidance. Cancer Theranostics. X. Chen and S. Wong (Eds): Elsevier Inc.; 2014. pp. 139–158. https://doi.org/10.1016/B978-0-12-407722-5.00009-8
67. Hong G, Diao S, Antaris AL, Dai H. Carbon nanomaterials for Biological Imaging and Nanomedicinal Therapy. Chem Rev. 2015;115:10816–906. https://doi.org/10.1021/acs.chemrev.5b00008.

68. Lefebvre TL, Brown E, Hacker L, et al. The potential of Photoacoustic Imaging in Radiation Oncology. Front Oncol. 2022;12:803777. https://doi.org/10.3389/fonc.2022.803777.
69. De La Zerda A, Zavaleta C, Keren S, et al. Carbon nanotubes as photoacoustic molecular imaging agents in living mice. Nat Nanotechnol. 2008;3:557–62. https://doi.org/10.1038/nnano.2008.231.
70. Patel U, Rathnayake K, Singh N, Hunt EC. Dual targeted delivery of Liposomal Hybrid Gold Nano-Assembly for enhanced Photothermal Therapy against Lung Carcinomas. ACS Appl Bio Mater. 2023;6:1915–33. https://doi.org/10.1021/acsabm.3c00130.
71. Ren Z, Cui J, Sun Q, et al. Polyethylene glycol—modified nanoscale conjugated polymer for the photothermal therapy of lung cancer. Nanotechnology. 2022;33:455101. https://doi.org/10.1088/1361-6528/ac85f4.
72. Chiang C-W, Chuang E-Y (2019) < p > Biofunctional core-shell polypyrrole–polyethylenimine nanocomplex for a locally sustained photothermal with reactive oxygen species enhanced therapeutic effect against lung cancer. Int J Nanomedicine Volume 14:1575–1585. https://doi.org/10.2147/IJN.S163299

Publisher's note